Available online at www.sciencedirect.com
SCIENCE DIRECT®
Acta Materialia 54 (2006) 2697–2704
Acta MATERIALIA
www.actamat-journals.com

Phase field simulation of equiaxed solidification in technical alloys

B. Böttger, J. Eiken, I. Steinbach *

RWTH–Aachen, Access e.V., Intzestrasse 5, 52072 Aachen, Germany

Received 17 October 2005; received in revised form 2 February 2006; accepted 8 February 2006
Available online 17 April 2006

Abstract

It is shown how the phase field method can be applied to simulate the equiaxed solidification of commercial alloys in technical processes. A multicomponent multiphase field model is coupled to thermodynamic databases. To handle the complex phase diagrams a local quasi-binary extrapolation is applied. Nucleation is treated by statistically distributed seed particles, taking into account the shielding of nucleation sites by recalescence, solute diffusion and growth of solid phases. To reduce computation time it is discussed how three-dimensional phenomena can be approximated by two-dimensional simulations, and the model for latent heat release is adjusted accordingly. As examples, simulations are presented of the commercial Mg–Al–Zn alloy AZ31, a hypereutectic Al–Si–Cu–Mg–Ni piston alloy and $AlCu_4Si_{17}Mg$.

Keywords: Solidification; Phase field models; Dendritic growth; Microstructure – equiaxed; Magnesium alloys

1. Introduction

Phase field models have recently become very popular for the simulation of microstructure evolution during solidification processes [1–5]. While these models address the evolution of a solid–liquid interface using only one phase field parameter, interaction of more than two phases or grains and consequently the occurrence of triple junctions needed to be included into the multiphase field approach [6–9].

Recent interest in the application of phase field simulations to industrial problems introduced a steeply increasing complexity regarding thermodynamics as well as thermal boundary conditions. Idealized descriptions of the phase diagram (ideal solution approximation [9], linear phase diagrams [7]) are in most cases not suitable for simulation of multicomponent multiphase systems. Instead, using Gibbs energy descriptions assessed from experiments by the CALPHAD approach [10] seems to be most promising [11]. Recently there have been alternative approaches suggested for using CALPHAD data via tie-line databases or other approximations [12–14].

Due to the size of the castings in industrial solidification processes, thermal gradients are typically quite low so that directional or columnar growth is observed only near the surface while the majority of the specimen is solidified by equiaxed growth. Hence – in contrast to Bridgman experiments – no stationary growth can be observed and the temperature during solidification is heavily influenced by latent heat.

The process of equiaxed dendritic solidification can be divided into two regimes. The first regime of free dendritic growth can be described analytically by the LGK model [15], and the second regime (dendritic interaction and recalescence) has been accounted for by a geometrical model for solute redistribution inside a spherical grain by Rappaz et al. [16]. The LGK model has subsequently been integrated into a numerical mesomodel of heat diffusion using the stagnant film approximation of the Ivantsov solution to link the length scales [17,18].

For the prediction of grain sizes, nucleation has to be taken into account. Statistical models starting from a given size distribution of inoculant particles which are based on

* Corresponding author. Tel.: +49 241 8098000; fax: +49 241 38578.
E-mail address: I.Steinbach@access.rwth-aachen.de (I. Steinbach).

1359-6454/$30.00
doi:10.1016/j.actamat.2006.02.008

free growth control of grain initiation [19] have been applied successfully, especially for aluminium alloys [20].

In this paper a multiphase field approach to equiaxed dendritic growth is presented which allows for direct coupling to thermodynamic databases with an arbitrary number of phases and components [21,22]. The nucleation model of Ref. [19] has been adapted and spatially discretized to describe the influence of seed density distribution, segregation and thermal boundary conditions on the grain size. Special care has been taken as regards the release of latent heat and its proper correction for two-dimensional (2D) simulations. The model is applied to a ternary magnesium model alloy and to two commercial four- and five-component aluminium alloys.

2. Multiphase field model for multicomponent alloys

2.1. Multiphase field equations

The phase field theory is an advanced computational approach which generally describes the evolution of so-called 'phase fields' $\Phi_\alpha(\vec{x},t),\ \alpha=1,\ldots,v$. In our model, these fields describe the distribution of either different phases or of grains with different orientations. If the respective phase or grain α locally exists $\Phi_\alpha=1$, else $\Phi_\alpha=0$. At the interfaces the phase field variable changes continuously from 1 to 0, thus the interfaces have a thickness η, which can be chosen to be large compared to the atomic interface thickness but small compared to the microstructure length scale. We start from a free energy formulation

$$F=\int_\Omega f^{\mathrm{IF}}+f^{\mathrm{CH}} \tag{1}$$

$$f^{\mathrm{IF}}=\sum_{\alpha,\beta=1}^{N}\frac{4\sigma_{\alpha\beta}}{\eta_{\alpha\beta}}\left(\frac{\eta_{\alpha\beta}^2}{\pi^2}|\nabla\Phi_\alpha\cdot\nabla\Phi_\beta|+W_{\alpha\beta}\right) \tag{2}$$

$$f^{\mathrm{CH}}=\sum_{\alpha=1}^{N}\Phi_\alpha f_\alpha(\vec{c}_\alpha)+\vec{\mu}\left(\vec{c}-\sum_{\alpha=1}^{N}\Phi_\alpha\vec{c}_\alpha\right) \tag{3}$$

The interface part f^{IF} is composed of all possible grain boundary contributions between phases α and β with the grain boundary energy $\sigma_{\alpha\beta}$ and the grain boundary width $\eta_{\alpha\beta}$. $W_{\alpha\beta}$ is the double obstacle potential $W_{\alpha\beta}=\Phi_\alpha\Phi_\beta$ for $0<\Phi_\alpha,\ \Phi_\beta<1$ and ∞ else. The chemical part f^{CH} within the interfaces and triple junctions is a linear mixture of the respective bulk contributions $f_\alpha(\vec{c}_\alpha)$, weighted by the local phase density that is identified to the phase field variable $\Phi_\alpha(\vec{x},t)$. μ is the generalized chemical potential that is introduced to conserve the local concentration (see below). The phase evolution in time is calculated by a set of phase field equations, deduced by minimization of pairwise free energy functionals $F_{\alpha\beta}(\Phi_\alpha,\nabla\Phi_\alpha)$ (for details see Refs. [6,8,21]). In the antisymmetric approximation the phase field equations read

$$\dot{\Phi}_\alpha=\sum_\beta\mu_{\alpha\beta}(\vec{n})\left[\sigma^*_{\alpha\beta}(\vec{n})K_{\alpha\beta}+w\Delta G_{\alpha\beta}(\vec{c})\right] \tag{4}$$

$$K_{\alpha\beta}=\Phi_\alpha\nabla^2\Phi_\beta-\Phi_\beta\nabla^2\Phi_\alpha+\frac{\pi^2}{\eta^2}(\Phi_\alpha-\Phi_\beta) \tag{5}$$

$$w=\frac{\pi}{\eta}\sqrt{\Phi_\alpha\Phi_\beta} \tag{6}$$

$$\Delta G_{\alpha\beta}=-f_\alpha(\vec{c}_\alpha)+f_\beta(\vec{c}_\beta)+\vec{\mu}(\vec{c}_\alpha-\vec{c}_\beta) \tag{7}$$

In this equation $\mu_{\alpha\beta}$ is the mobility of the interface as a function of the interface orientation (here described by the interface normal vector $\vec{n}$). $\sigma^*_{\alpha\beta}$ is the effective anisotropic surface energy (surface stiffness) and $K_{\alpha\beta}$ is related to the local curvature of the interface. The interface is driven by the curvature contribution $\sigma^*_{\alpha\beta}K_{\alpha\beta}$ on the one hand and the thermodynamic driving force $\Delta G_{\alpha\beta}$ on the other hand, where the function w was introduced to concentrate the driving force to the centre of the interface. In most solidification processes the movement of the interface is controlled by a competition of these two contributions having opposite signs. The thermodynamic driving force is a function of the local composition and couples the phase field equations to the diffusion equations.

2.2. Diffusion equations

In contrast to sharp interface models, where all phases are clearly separated, in the phase field model the interface is treated as a mixture of the adjacent phases. The description of composition and solute diffusion for the diffuse interface where multiple phases coexist is a fundamental problem. In the present model we allow all coexisting phases α to have different compositions $\vec{c}_\alpha$. The components of these composition vectors $\vec{c}_\alpha$ are the concentrations c_i^α of the k solute components. The total concentration $\vec{c}$ of the phase mixture at a location $\vec{\mathbf{x}}$ is given by the sum of the individual phase concentrations weighted by the respective phase field parameter [7]:

$$\vec{c}(\vec{\mathbf{x}})=\sum_{\alpha=1}^{N}\Phi_\alpha(\vec{\mathbf{x}})\vec{c}_\alpha(\vec{\mathbf{x}}) \tag{8}$$

The total concentrations $\vec{c}$ are conserved parameters and Eq. (8) is the local mass balance. To solve transport and redistribution a set of k coupled diffusion equations are deduced from the free energy functional [21]:

$$\dot{\vec{c}}=\nabla\sum_{\alpha=1}^{N}\Phi_\alpha\mathbf{D}_\alpha\nabla\vec{c}_\alpha(\Phi_\beta,\vec{c}) \tag{9}$$

with $\mathbf{D}_\alpha$ being the multicomponent diffusion coefficient matrix for phase α. The required phase concentrations $\vec{c}_\alpha$ can be determined from the phase field parameters and the total concentrations using the constraint of mass balance (Eq. (8)) and additionally the constraint of quasi-equilibrium. This constraint postulates that all reduced chemical potentials μ_α^i (defined as the chemical potentials of solute components i minus the chemical potential of the solvent component) are the same for coexisting phases (see also Ref. [4]):

$$\vec{\mu}_\alpha(\vec{c}_\alpha(\vec{\mathbf{x}}))=\vec{\mu}_\beta(\vec{c}_\beta(\vec{\mathbf{x}}))\quad\forall\alpha,\beta \tag{10}$$

2.3. Extrapolation of multiphase multicomponent data

The quasi-equilibrium phase concentrations that are required to solve the diffusion and the phase field equations can generally be derived from thermodynamic calculations using approved databases. However, doing this in every time-step for all interface cells is very time-consuming. To speed up simulations, thermodynamic calculations are only run at certain time-steps and interpolated between. The criteria for running the thermodynamic calculations have to be specified by the user, e.g., by specifying temperature or time intervals. The calculations are also done if a new phase is nucleated and therefore the thermodynamic description changes significantly. Starting from a set of quasi-equilibrium phase concentrations $\vec{c}^{\,*}_{\alpha}$ and the respective temperature T^* for each pairwise phase interaction in each cell of the numerical grid, a new set of $\vec{c}_{\alpha}$ is extrapolated. Using the abbreviations $\Delta\vec{c}_{\alpha}$, $\Delta\vec{c}_{\beta}$ and ΔT for the differences between extrapolated and starting values, the quasi-equilibrium constraint is considered by

$$\Delta\vec{c}_{\beta} = \mathbf{k}_{\beta\alpha}\Delta\vec{c}_{\alpha} + \vec{q}_{\beta\alpha}\Delta T \tag{11}$$

with

$$k^{ij}_{\beta\alpha} = \left(\frac{\partial c^{j}_{\beta}}{\partial c^{j}_{\alpha}}\right)_{c^{k\neq i}_{\alpha},T}, \quad \vec{q}_{\beta\alpha} = \left(\frac{\partial\vec{c}_{\beta}}{\partial T}\right)_{c_{\alpha}} \tag{12}$$

where $\mathbf{k}_{\beta\alpha}$ is the quasi-equilibrium partition matrix and the vectors $\vec{q}_{\alpha\beta}$ and $\vec{q}_{\beta\alpha}$ are concentration slopes with respect to temperature. Their coefficients are evaluated and stored from thermodynamic quasi-equilibrium calculations, varying the concentrations c^{i}_{α} and the temperature independently. Applying this relationship for all phases together with Eq. (8), new phase concentrations $\vec{c}_{\alpha}$ can be extrapolated for changed phase field parameters, changed total concentrations and changed temperatures from the starting set of phase concentrations $\vec{c}^{\,*}_{\alpha}$ by

$$\begin{aligned}
&\vec{c}_{\alpha}(\vec{c},\Phi_{\beta},T) = \mathbf{k}^{-1}_{\alpha c}\vec{c} - \vec{c}^{\,*}_{\alpha c}(\Phi_{\beta},T)\\
&\text{with}\quad \mathbf{k}_{\alpha c} = \sum_{\beta}^{N}\Phi_{\beta}\mathbf{k}_{\beta\alpha}\\
&\text{and}\quad \vec{c}^{\,*}_{\alpha c} = \sum_{\beta}^{N}\Phi_{\beta}(\vec{c}^{\,*}_{\beta} - \mathbf{k}_{\beta\alpha}\vec{c}^{\,*}_{\alpha} + \vec{q}_{\beta\alpha}\Delta T)
\end{aligned} \tag{13}$$

For alloys with low cross dependencies between the solute components, the computational effort can further be reduced by neglecting the off-diagonal terms of the partition matrix $\mathbf{k}_{\beta\alpha}$, which we call multibinary extrapolation. The model is described in more detail elsewhere [21].

2.4. Model of hexagonal crystallographic anisotropy

In magnesium-based alloys the hexagonal lattice symmetry of the dominant hexagonal close-packed phase leads to a morphology which is different from the typical cubic dendrites observed in most technical alloys with dominant face-centred cubic (fcc) or body-centred cubic phases. To simulate the growth of this phase, hexagonal anisotropy functions have to be integrated into the model. A general form of the anisotropy function with equal strength of anisotropy in the basal and in normal direction is given by

$$d_{\text{hex}} = 1 + \delta_{\text{hex}}(n_x^6 - 15n_x^4n_y^2 + 15n_x^2n_y^4 - n_y^6 + 5n_z^4 - 5n_z^2 + 6n_z^6) \tag{14}$$

where δ_{hex} is the anisotropy coefficient, $\vec{n}$ being a unit vector normal to the interface transformed into the local grain coordinate system. This function is visualized in Fig. 1 (left). It describes six prism orientations in the xy-plane and two basal orientations in the z-direction. According

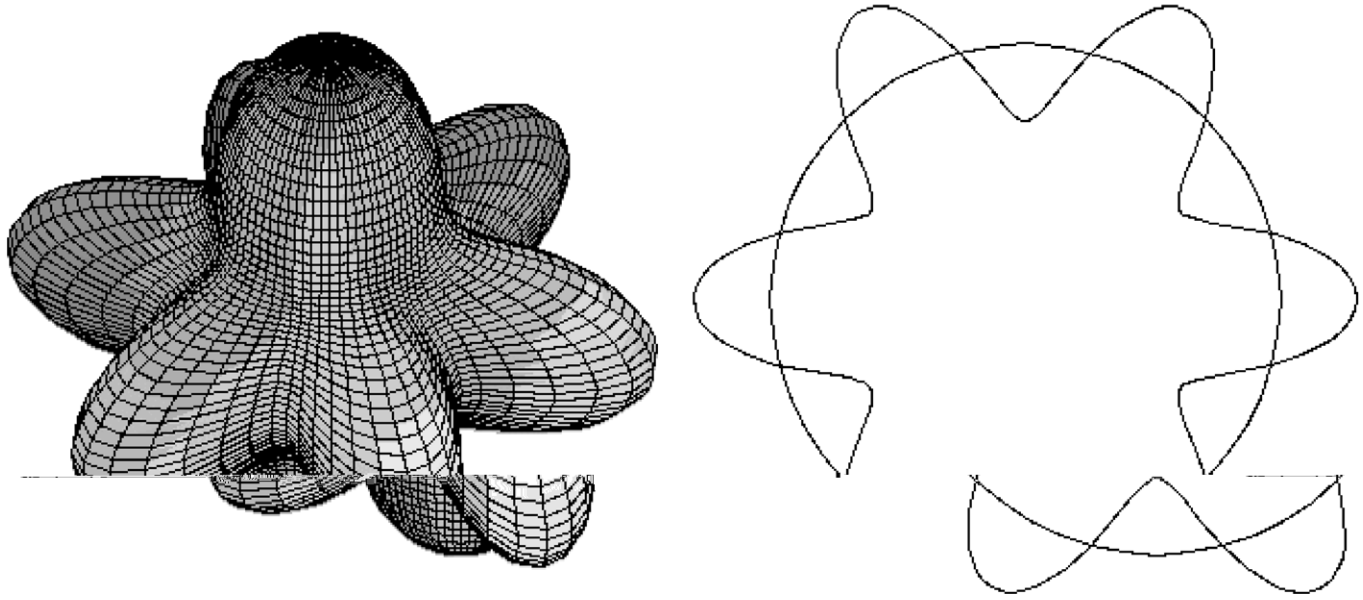

Fig. 1. Hexagonal anisotropy function for the interface mobility (left) and 2D cut (right).

to experimental observation there is a strong dominance of prism orientations. Therefore in 2D simulations the xy-cut of the anisotropy function is selected. In this case the function is reduced to

$$d_{\mathrm{hex}}^{\mathrm{2D}} = 1 + \delta_{\mathrm{hex}} \cos(6\phi) \tag{15}$$

where ϕ is the angle between the surface normal and the first prismatic direction. The anisotropic interface mobility is described in 2D by

$$\mu_{\alpha\beta}(\phi) = \mu_0 d_{\mathrm{kin}}(\phi) \tag{16}$$

where d_{kin} is the kinetic anisotropy function. With the static anisotropy coefficient δ_{st} we define the anisotropy of the surface energy $\sigma_{\alpha\beta}$ and surface stiffness $\sigma^*_{\alpha\beta}$ used in Eq. (4):

$$\sigma_{\alpha\beta} = \sigma_0 d_{\mathrm{st}} = \sigma_0(1 + \delta_{\mathrm{st}} \cos(6\phi)) \tag{17}$$

and the effective surface energy (surface stiffness) is calculated by

$$\sigma^*_{\alpha\beta} = \sigma_{\alpha\beta} + \frac{\partial^2 \sigma_{\alpha\beta}}{\partial \phi^2} = \sigma_0(1 - 35\delta_{\mathrm{st}} \cos(6\phi)) \tag{18}$$

This pragmatic treatment of the anisotropic surface energy gives adequate results in 2D; however, for the three-dimensional (3D) case an appropriate treatment is not yet available. The additional effect of a concentration dependence of the surface energy is not included in the calculation; however, the surface energy coefficients between different phases can be chosen individually in the model. The anisotropy model for faceted growth of silicon particles is described elsewhere [23].

3. Boundary conditions for equiaxed growth

3.1. Temperature evolution

In equiaxed solidification temperature evolution is directly linked to the local microstructure growth. Therefore in phase field simulation temperature cannot be described a priori. Thermal diffusion can be considered as much faster than solute diffusion. In fact, if the thermal diffusion is taken to be longer than the size of the calculation domain and if there are no (or at least no strong) thermal gradients (i.e. heat extraction is isotropic in all directions), latent heat can be just averaged inside the simulation domain and be used to obtain the global temperature evolution:

$$\dot{T} = \frac{1}{\overline{C}_{\mathrm{p}}} \left(-\frac{\dot{Q}}{V} \mathrm{d}t + \sum_{\alpha} H_\alpha \dot{f}_\alpha \right) \tag{19}$$

where $\dot{Q}/V$ is the volume heat extraction rate, H_α is the enthalpy per volume of phase α, $\overline{C}_p$ is the specific heat averaged over the N_{xyz} cells of the numerical grid and $\dot{f}_\alpha$ is the averaged rate of change of the phase α:

$$\overline{C}_p = \sum_{\alpha} C_{p,\alpha} \frac{\sum_{xyz} \Phi_\alpha}{N_{xyz}} \tag{20}$$

$$\dot{f}_\alpha = \frac{\sum_{xyz} \dot{\Phi}_\alpha}{N_{xyz}} \tag{21}$$

These relations introduce the connection between the phase field equation and heat extraction, which will result in a recalescence phenomenon, if the release of latent heat during fast growth after nucleation exceeds the heat extraction, as commonly observed in equiaxed solidification processes.

3.2. 2D simulation

Although the phase field method is an excellent tool for 3D simulations, in most cases the restrictions in memory size and calculation time will favour 2D simulations whenever there is a chance to transform the 2D results to 3D. This transformation can be very obvious as in the case of a planar lamellar eutectic structure where one dimension is just the expansion of a cut perpendicular to the lamellae. In equiaxed solidification this transformation is more difficult as none of the three dimensions is distinguished from the others.

In general one can construct the 2D domain either as a cut through the structure or as a projection of the 3D structure onto 2D. In the first case, e.g., if we have various small particles growing from the melt, we will find only a few of them in the 2D cut and the mean distance between the particles will not be correct. Therefore the interaction of the diffusion fields would not be described well in such a simulation. In the second case – by projecting particles onto the 2D plane which are nearer to the plane than the average particle distance – we are able to transform correctly the average particle distance to the 2D domain. However, as a consequence the average phase fractions will be wrong in 2D and as such the release of latent heat is not correct.

In the early state of solidification, when the solid fraction is small and the growing structures are far apart, we can neglect solutal interactions between the structures. This is perfectly the case for the initial state in nucleation. Then a geometrical correction for the dimensionality can be applied to the observed phase fractions in the projection plane. The following formula is proposed for the correction of the phase fractions to a 3D equivalent fraction f^*_α:

$$f^*_\alpha = \left(\frac{f_\alpha}{f_{\mathrm{M}} + f_\alpha} \right)^{3/2} (f_{\mathrm{M}} + f_\alpha) \tag{22}$$

In this equation f_α denotes the phase fractions obtained from the 2D simulation and f_{M} is the fraction of a matrix phase which in the case of solidification is the melt. f^*_α replaces f_α in Eq. (19). This correction greatly affects the release of latent heat during the initial part of solidification where the selection of the grain size is taking place.

4. Nucleation

Under equiaxed growth conditions nucleation is a very important parameter for microstructure formation as continuous growth is not possible as in directional solidification. If the melt is not extremely pure as in the case of technical alloys, formation of the primary phases is dominated by heterogeneous nucleation. In order to get a small

grain size and to suppress columnar growth, small particles are commonly added as nucleation agents. This inoculation provides well-defined starting points for nucleation with a given undercooling:

$$\Delta T_{\mathrm{Nuc}} = \frac{4\gamma}{\Delta S d} \tag{23}$$

where ΔS is the entropy of fusion, d the particle diameter and γ the solid–liquid interfacial energy [19].

4.1. Analytical curvature model

If a particle is smaller than the numerical interface thickness, the phase field algorithm is no longer able to evaluate the correct curvature of this particle. In typical castings grain sizes can be of the order of several hundreds of micrometres while inoculants are much smaller (often less than 1 μm). So without special algorithms like grid refinement they cannot be reasonably resolved. For that reason inoculants, which can have a very small diameter compared to the equidistant grid spacing Δx used in our simulation, are assumed to be spherical and treated using an analytical expression for the curvature. The curvature term $K_{\alpha\beta}$ in Eq. (4)

$$K_{\alpha\beta} = \Phi_\alpha \nabla^2 \Phi_\beta - \Phi_\beta \nabla^2 \Phi_\alpha + \frac{\pi^2}{\eta_{\alpha\beta}^2}(\Phi_\alpha - \Phi_\beta) \tag{24}$$

is replaced by the corresponding analytical term

$$K_{\alpha\beta} = 2/r\Delta x \tag{25}$$

where r is the radius calculated from the phase field parameter Φ in the reference cell, where the 'small grain' is located, by

$$r = \frac{\Phi}{4/3\pi^{1/3}}\Delta x \tag{26}$$

As ϕ is increasing during growth of the particle, the analytical regime of Eq. (25) is linearly transferred to the 'phase field regime' (Eq. (24)).

4.2. Seed density model

The effectiveness of inoculants for grain refinement is not only defined by their maximum particle sizes but also by their particle size distribution. When heat is extracted from the melt the biggest particles will first nucleate at an undercooling defined by their radius (assuming complete wetting or using an effective seed radius instead). As they start growing and releasing latent heat immediately they start interacting with other potential nucleation precursors. Depending on the heat extraction rate and the number and sizes of all the other seeding particles, the temperature will drop more or less well below the liquidus temperature thereby defining the number of seeds that will be activated.

Therefore the seed density–radius distribution is used together with the analytical curvature model in Section 4.1 for the prediction of precipitation densities or final grain sizes. In Fig. 2 the results of a simulation can be seen for an $AlCu_4Si_{17}Mg$ alloy showing nucleation of primary silicon particles from the melt for two different heat extraction rates. A seed density distribution chosen to demonstrate the cooling rate dependence under typical casting

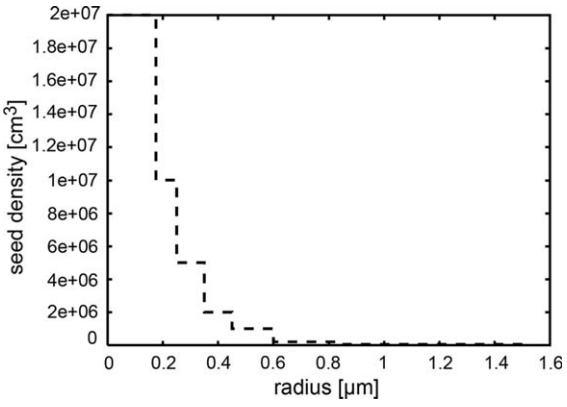

Fig. 3. Assumed radius distribution of inoculant particles for Fig. 2.

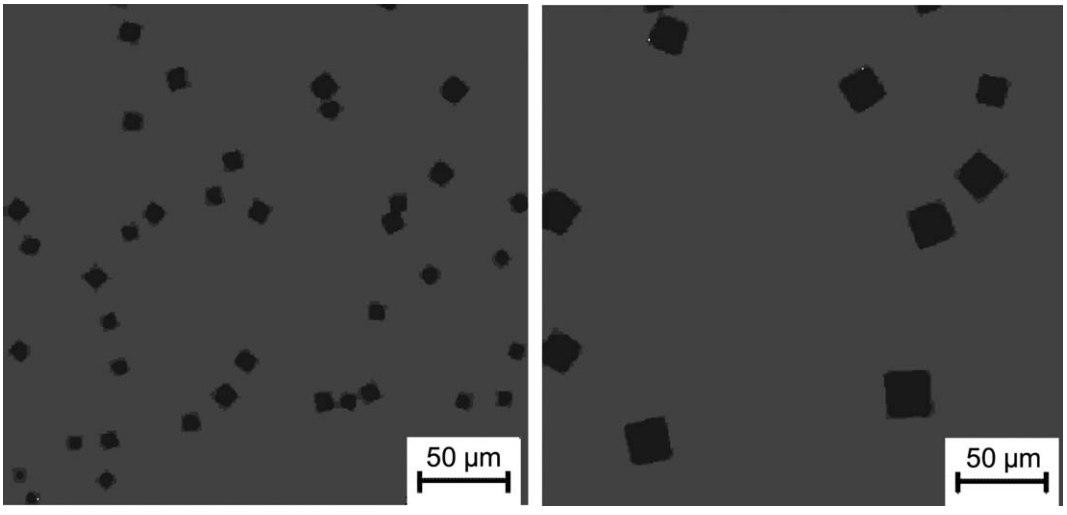

Fig. 2. Simulation of primary silicon nucleation in $AlCu_4Si_{17}Mg$, showing the dependency of the final particle number on the volume heat extraction rate (right: -15 J/cm^3; left: -60 J/cm^3).

conditions has been used (see Fig. 3). As can be clearly seen, a higher number of faceted silicon particles is predicted to grow at a higher heat extraction rate.

5. Application to the Mg–Al–Zn alloy AZ31

The most frequently used magnesium alloys for industrial production are Mg–Al-based alloys. Additions of zinc and manganese lead to the AZ and AM alloys, respectively. In this paper simulations of equiaxed solidification of AZ31 (Mg–3% Al–1% Zn) are presented. For the improvement of both mechanical properties as well as castability, grain refinement is an important issue. The seed density model has been applied to the primary magnesium phase in the simulation shown in Fig. 4. The calculations start with a homogeneous melt at a given temperature. The upper left panel shows the reference calculation for the AZ31 alloy. Three different modifications – variation of the composition (upper right), the seed density function (lower left) and the heat extraction rate (lower right) – have been applied to demonstrate the general ability of the model to reproduce qualitatively different grain refining mechanisms. As can be seen in all three cases the number of grains predicted by simulation is greater than that of the reference simulation. It should be noted that the predicted dendritic morphology is also affected by these modifications. While the composition change (increase of aluminium content) did not significantly change the dendrite shapes, increasing the seed density resulted in more globular grains. In contrast, increasing the heat extraction rate for the given seed density distribution leads to more dendritic grains.

For a quantitative comparison, data for the radius distribution of the seeding particles must be known, which can be deduced indirectly by calibration using experiments with different cooling parameters.

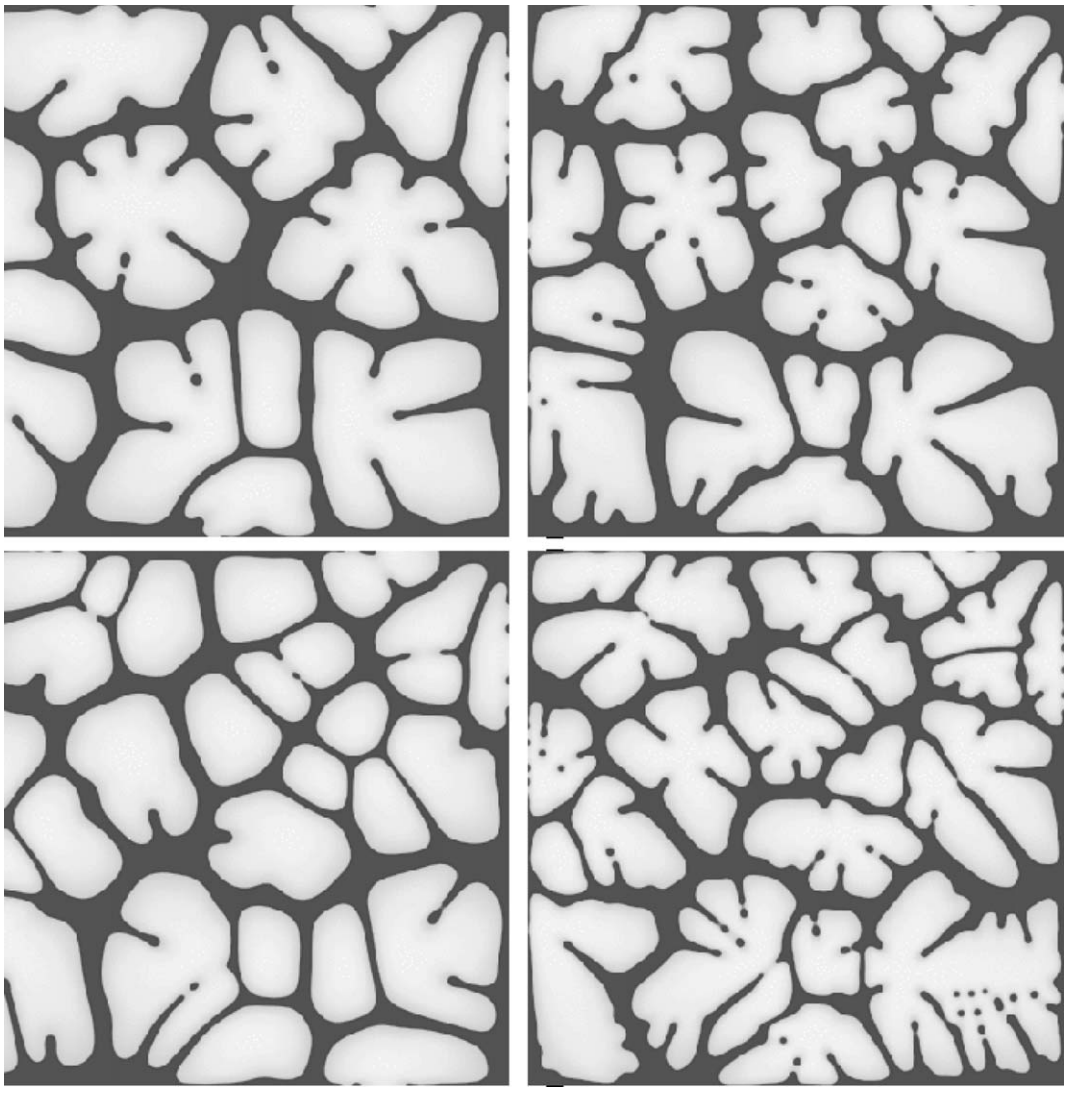

Fig. 4. Simulations of equiaxed solidification with parameter variation: AZ31 (upper left); enhanced aluminium concentration (upper right); enhanced number of inoculant particles (lower left); enhanced heat extraction rate (lower right).

6. Application to the commercial aluminium alloys KS1295 and $AlCu_4Si_{17}Mg$

Fig. 5 shows a comparison between the simulated and experimental microstructure of the typical hypereutectic piston alloy KS1295. In this case the focus is on the dendrite arm spacing (DAS) and its relation to the local solidification time. A constant heat extraction rate of 15 J/cm^3 has been applied and as in the case of $AlCu_4Si_{17}Mg$ (Fig. 2), the seed density model has been applied for nucleation of primary silicon particles. During growth of the primary silicon the melt is depleted in silicon. Reaching the eutectic composition, one would expect that solidification terminates in a eutectic mode. However, since the crystal lattices of silicon and the fcc aluminium phase are quite different, nucleation of the fcc aluminium phase on the silicon particles requires a very high undercooling and therefore was disabled in the simulation. Instead it was assumed that fcc aluminium would nucleate heterogeneously with an assumed undercooling of 2 K. In order to fix the grain size of the fcc aluminium the nucleation points were set in the corners of the calculation domain. For the same reason as above, the nucleation of silicon on the fcc aluminium phase is also difficult and was allowed only with a high critical undercooling of 15 K. Therefore the fcc aluminium phase can grow in a dendritic manner. Nucleation of Mg_2Si (black particles in Fig. 5) has been included in the simulation with a nucleation undercooling of 5 K on the fcc aluminium surface; however, this phase becomes thermodynamically stable only well below the Al–Si eutectic temperature. As no experimental data are available for the nucleation parameters, reasonable assumptions had to be made in accordance with experimental microstructures. In particular the sequence of solid phases, primary silicon – fcc aluminium – secondary silicon – Mg_2Si, that indicates a pronounced non-equilibrium solidification path, could be reproduced by the simulations close to the experimental observation. Fig. 6 shows the results for the DAS from several simulations with varied heat extraction rate and therefore different solidification times as well as from a real piston alloy. Double-logarithmic fitting shows typical behaviour for this type of alloy. The resulting criterion function can be used for process optimization on the macroscale.

Fig. 7 shows the resulting microstructure after complete solidification for the alloy $AlCu_4Si_{17}Mg$. Compared to KS1295, much bigger primary silicon particles are observed in accordance with the higher silicon content. As a consequence of the bigger difference between the liquidus temperature of silicon and the dendritic fcc aluminium phase, there is much less interaction between the two growing phases compared to KS1295, where the size and density of the primary silicon particles are heavily influenced by the dendrites (Fig. 5). Furthermore in Fig. 7 eutectic silicon (grey rods), Mg_2Si (black) and θ-AlCu (grey) can be seen.

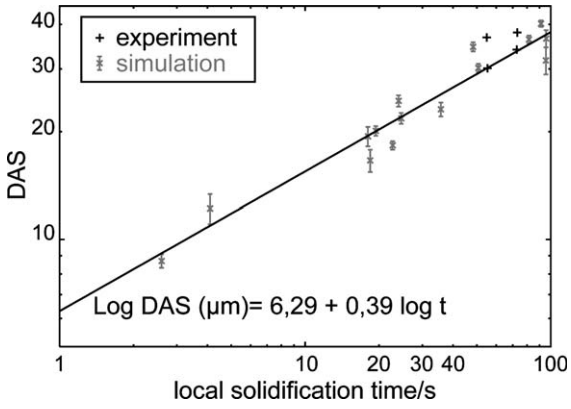

Fig. 6. Relation between average DAS and local solidification time from simulations with varying heat extraction rate.

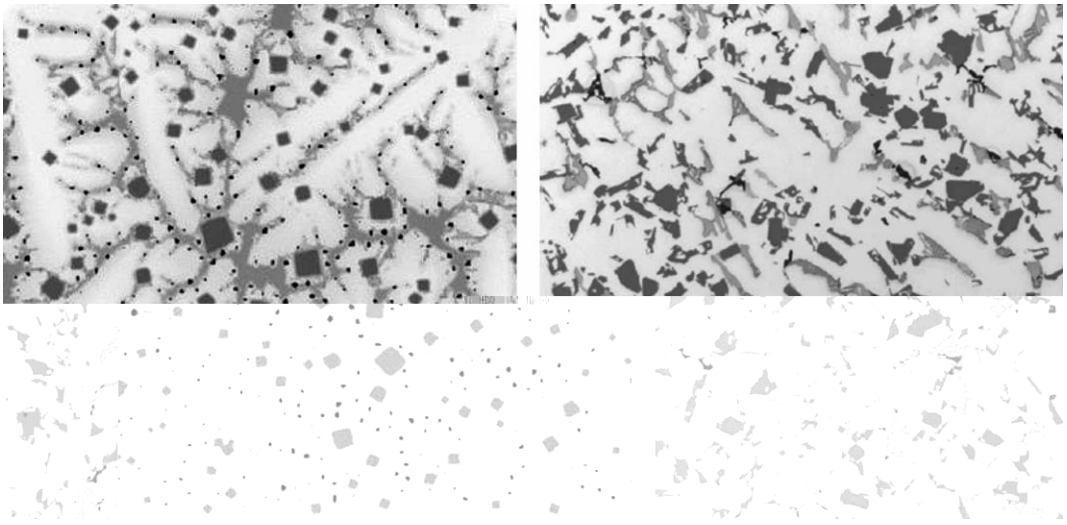

Fig. 5. Comparison between simulation (left) and experiment (right) for KS1295. The area is 400 µm × 400 µm in both images, but the exact temperature history in the experiment is not known accurately for a quantitative comparison.

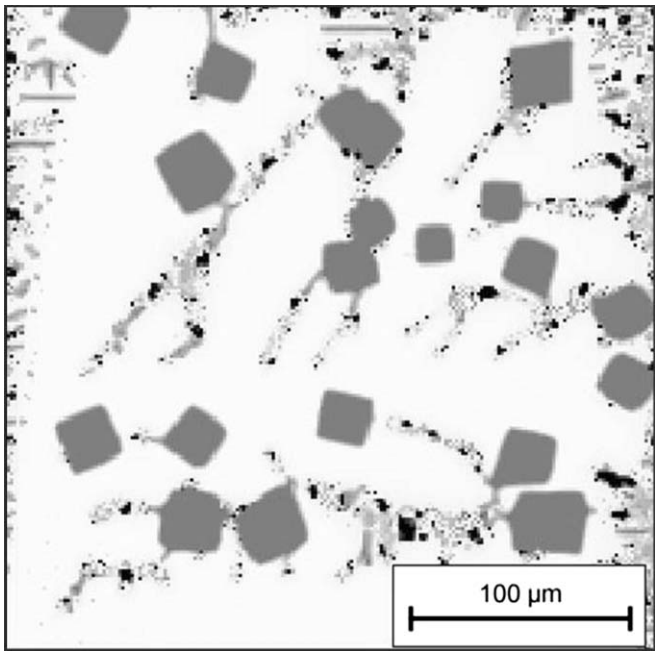

Fig. 7. Solidification microstructure of $AlCu_4Si_{17}Mg$.

Obviously the eutectic phases are not properly resolved in this simulation. Eutectic morphologies should be investigated at a different length scale.

7. Conclusion

It has been shown that the phase field method coupled to thermodynamic databases can be a valuable tool for simulating equiaxed solidification processes in technical alloys. Qualitative effects like the different grain refining mechanisms and their effect on the grain size and dendritic morphology in AZ31, the effect of the heat extraction rate on the DAS in KS1295 or the relation between alloy composition and microstructure ($AlCu_4Si_{17}Mg$ vs. KS1295) have been shown. Due to the complexity of the systems the results would not always have been expected, as in the case of the complex interactions between primary silicon and the aluminium dendrites in KS1295. The major problem for obtaining quantitative results is the lack of physical parameters such as the surface energies, the diffusion coefficients and the critical nucleation undercoolings or seed density curves for the different phases. Quantitative information cannot be obtained without intensive calibration using solidification experiments, which have to be performed under well-determined conditions. Then, in addition to the qualitative understanding of the complex mechanisms of microstructure formation, a quantitative prediction of certain microstructural quantities (like the DAS) and their dependence on the local conditions or on the alloy composition is possible.

Acknowledgement

We acknowledge funding by the German Research Foundation (DFG) in the Priority Programme SPP-1168.

References

[1] Kobayashi R. Physica D 1993;63:410.
[2] Wheeler AA, Boettinger WJ, McFadden GB. Phys Rev A 1992;45:7424.
[3] Caginalp G, Xie W. Phys Rev E 1993;48:1897.
[4] Kim SG, Kim WT, Suzuki T. Phys Rev E 1999;60:7186.
[5] Karma A, Lee YH, Plapp M. Phys Rev E 2000;61:3996.
[6] Steinbach I, Pezzolla F, Nestler B, Seeelberg M, Prieler R, Schmitz GJ, et al. Physica D 1996;94:135.
[7] Tiaden J, Nestler B, Diepers HJ, Steinbach I. Physica D 1998;115:73.
[8] Steinbach I, Pezzolla F. Physica D 1999;134:385.
[9] Nestler B, Wheeler AA. Physica D 2000;138:114.
[10] Saunders N, Miodownik A. CALPHAD calculation of phase diagrams: a comprehensive guide. Elsevier; 1998.
[11] Grafe U, Böttger B, Tiaden J, Fries SG. Scripta Mater 2000;42:1179.
[12] Qin RS, Wallach ER. Acta Mater 2003;51:6199.
[13] Kobayashi H, Ode M, Kim SG, Kim WT, Suzuki T. Sripta Mater 2003;48:689.
[14] Wu K, Chang YA, Wang Y. Scripta Mater 2004;50:1145.
[15] Lipton J, Glicksman ME, Kurz W. Mater Sci Eng 1984;65:57.
[16] Rappaz M, Thévoz Ph. Acta Metall 1987;35:1487.
[17] Steinbach I, Kauerauf B, Beckermann C, Guo J, Li Q. Acta Mater 1999;47:971.
[18] Steinbach I, Diepers H-J, Beckermann C. J Cryst Growth 2005;275:624.
[19] Quested TE, Greer AL. Acta Mater 2004;52:3859.
[20] Greer AL, Cooper PS, Meredith MW, Schneider W, Schuhmacher P, Spittle JA, et al. Adv Eng Mater 2003:81.
[21] Eiken J, Böttger B, Steinbach I. Phys Rev E, to be published.
[22] www.micress.de.
[23] Steinbach I, Pezzolla F, Prieler R. Modelling of casting, welding and advanced solidification processes VII. Warrendale (PA): TMS; 1995. p. 695.